Paracrine enhancement of tumor cell proliferation provides indirect stroma-mediated chemoresistance via acceleration of tumor recovery between chemotherapy cycles.

Daria Miroshnychenko*[1], Tatiana Miti*[3], Anna Miller[3], Pragya Kumar[1,8], Mark Laurie[6], Marilyn M. Bui[4], Philipp M. Altrock[5], David Basanta**[3,7], Andriy Marusyk**[1,2]

Affiliations:

1. Department of Cancer Physiology, H Lee Moffitt Cancer Center and Research Institute, Tampa, FL, USA.
2. Department of Molecular Medicine, University of South Florida, Tampa, FL, USA.
3. Department of Integrated Mathematical Oncology, H Lee Moffitt Cancer Center and Research Institute, Tampa, FL, USA.
4. Department of Pathology, H. Lee Moffitt Cancer Center and Research Institute, Tampa, FL, USA.
5. Department of Evolutionary Theory, Max Planck Institute for Evolutionary Biology, Ploen, Germany
6. Summer Undergraduate Program to Advance Research Knowledge, H Lee Moffitt Cancer Center and Research Institute, Tampa, FL, USA.
7. Department of Molecular Biosciences, University of South Florida, Tampa, FL, USA.
8. University of South Florida Cancer Biology PhD Program, Tampa, FL, USA

*, ** These authors contributed equally to the study

Abstract.

The ability of tumors to survive therapy is mediated not only by cell-intrinsic but also cell-extrinsic, microenvironmental mechanisms. Across many cancers, including triple-negative breast cancer (TNBC), a high stroma/tumor ratio correlates with poor survival. In many contexts, this correlation can be explained by the direct reduction of therapy sensitivity by stroma-produced paracrine factors through activating pro-survival signaling and stemness. We sought to explore whether this direct effect contributes to the link between stroma and poor responses to chemotherapies in TNBC. Our *in vitro* studies with panels of TNBC cell line models and stromal isolates failed to detect a direct modulation of chemoresistance. However, we found that fibroblasts often enhance baseline tumor cell proliferation. Consistent with this in vitro observation, we found evidence of stroma-enhanced TNBC cell proliferation *in vivo,* in xenograft models and patient samples. Based on these observations, we hypothesized an indirect link between stroma and chemoresistance, where stroma-augmented proliferation potentiates the recovery of residual tumors between chemotherapy cycles. To test this hypothesis, we developed a spatial agent-based model of tumor response to repeated dosing of chemotherapy. The model was quantitatively parameterized from histological analyses and experimental studies. We found that even a slight enhancement of tumor cell proliferation within stroma-proximal niches can strongly enhance the ability of tumors to survive multiple cycles of chemotherapy under biologically and clinically feasible parameters. In summary, our study uncovered a novel, indirect mechanism of chemoresistance. Further, our study highlights the limitations of short-term cytotoxicity assays in understanding chemotherapy responses and supports the integration of experimental and *in silico* modeling.

Introduction

For many types of cancers, standard cytotoxic chemotherapy remains the main treatment option. Chemotherapies produce strong systemic toxicities but often fail to cure the cancers, especially in advanced, metastatic stages. Improving the clinical outcomes of these therapies requires an adequate understanding of the mechanisms responsible for treatment failure. The ability of some of the tumors to persist through therapies is typically attributable to cell-intrinsic genetic and epigenetic mechanisms that impact drug sensitivity. At the same time, the chemosensitivity of tumors might also reflect cell extrinsic, microenvironmental factors. Across many types of cancers, high stroma-to-tumor ratios correlate with poor outcomes (1–7). In multiple contexts of targeted therapy, this correlation appears to reflect a direct microenvironmentally mediated persistence/resistance. For example, paracrine factors produced by cancer-associated fibroblasts (CAFs) and other non-malignant cell types within the tumor microenvironment (TME), can strongly blunt the sensitivity of cancer cells to inhibition of oncogenic drivers by the activation of alternative signaling pathways and the induction of cell plasticity (8). However, the relevance of direct desensitization toward chemotherapy sensitivity is less clear.

We sought to explore the link between stroma and chemotherapy responses in triple-negative breast cancers (TNBC), where stromal gene expression signature is linked to poor chemotherapy responses (9). Despite the developments in immune therapies and the recent approval of PARP inhibitors and antibody-drug conjugates, cytotoxic chemotherapies remain the primary therapeutic tool for adjuvant and neoadjuvant TNBC therapy. The most commonly used treatment modality in the US is a dose-dense therapy that includes anthracyclines (such as doxorubicin), cyclophosphamide, and taxanes (AC-T regimen). Chemotherapy is administered intravenously

either as an injection over a few minutes, or as infusions over a few hours. Two to three-week breaks are given to allow patients to recover from the strong side effects of the treatment. This cycle is repeated several times. TNBC tumors are typically sensitive to chemotherapy, and this sensitivity is maintained over the course of the treatment (10), suggesting that TNBC can avoid therapeutic elimination without acquiring *bona fide* resistance (11), as long as a sufficient number of tumor cells can survive till the end of chemotherapy.

Like several other cancer types, high stromal content in TNBC strongly correlates with poor prognosis (7,9,12). Moreover, stromal gene expression signatures predict a diminished response to the anthracycline-containing chemotherapeutic regimen in neoadjuvant therapy (9), suggesting a causal link between stroma and therapy persistence. However, we failed to observe a direct chemoprotection. Instead, we found that, often, CAFs and CAF-conditioned media (CAF CM) enhance the proliferation of TNBC cells *in vitro,* irrespective of the treatment. Consistent with these observations, we found that proximity to stroma is associated with enhanced tumor cell proliferation *in vivo*, in xenograft models and clinical samples. These findings led us to hypothesize an indirect link between stroma and chemoresistance: the ability of tumors to avoid therapy-induced extinction is mediated by an accelerated recovery of residual tumors between cycles of chemotherapy. To test the feasibility of this hypothesis, we developed a mathematical model (a spatial agent-based model (ABM)), parameterized and calibrated with experimental data, to understand the impact of stroma-enhanced proliferation on the cancer cell population dynamics. We found that a relatively modest enhancement of cell proliferation within stroma-proximal tumor cells is sufficient to substantially decrease the probability of therapeutic extinction. These findings indicate the existence of a new type of chemoresistance mechanism that likely contributes to the ability of a subset of tumors to persist through therapy and might be suppressed therapeutically.

Results

CAFs stimulate the proliferation of TNBC cells but provide no direct chemoprotection.

CAFs are one of the main cellular components of the tumor microenvironment (TME), and the primary producer of extracellular matrix (ECM), growth factors, and cytokines. Multiple cytokines and ECM components, produced by CAFs (e.g., HGF, FGFs, fibronectin, *etc*.) have been shown to strongly reduce the sensitivity of cancer cells to therapeutic agents in multiple contexts of targeted and cytotoxic therapies (6,13–16). Therefore, we asked whether the known correlation between poor prognosis and high stromal gene signature can be reduced to a correlation with CAFs. To this end, using the KM plotter tool (17) (see Methods), we interrogated publicly available expression datasets to explore the association between the expression of CAF markers and TNBC survival. We found that the expression of individual CAF markers αSMA, FAP, and PDGFRa, was associated with significantly lower survival (**Fig. S1**). This association led us to speculate that, like other contexts of CAF-mediated therapy resistance (18,19), CAFs might directly reduce the sensitivity of TNBC cells to chemotherapeutic agents. To test this hypothesis, we evaluated the ability of CAFs to modify the sensitivity of a panel of TNBC cell lines to the ACT components doxorubicin and taxol, as well as the widely used therapeutic agent cisplatin. Since the commonly used viability assays, such as CellTiterGlo or MTT cannot discriminate between the viability signals of cancer cells and CAFs, we used luciferase-labeled TNBC cells and bioluminescence readout, as described in our prior work (20) (**Fig. 1A**). When normalized to vehicle-treated TNBC cell monocultures (**Fig. 1B**), co-culture with CAFs enhanced the luminescence readout under treatment in most of the tested models (**Fig. 1C**). However, we also observed a substantially higher luciferase signal in the DMSO controls of the CAF co-cultures, suggesting a general enhancement of proliferation, rather than reduction of sensitivity to therapy. Indeed, when the readouts of the CAF co-cultures were normalized separately to their DMSO controls (**Fig. 1B**), luciferase signal enhancement under therapy was no longer observed (**Fig 1D**). Notably, this lack of specific protection stands in contrast to the CAF-mediated desensitization to the therapies that target specific signaling nodes, such as EGFR/HER2 inhibitor lapatinib, reported in our prior work (20), or pan-class I PI3K inhibitor BKM120 (**Fig. S2A)**.

A general enhancement of the luciferase signal was also observed with a large panel of primary human CAFs, normal breast fibroblasts, and immortalized and primary mouse fibroblasts (**Fig. S2B, C**). The effect of CAFs was phenocopied with CAF-conditioned media (CM), suggesting mediation by secreted factors (**Fig 1E**). To address whether the enhanced luciferase signal observed with CAF co-cultures and CM reflected enhanced cell proliferation, we used time-lapse microscopy, with TNBC labeled with nuclear GFP, as described in our prior work (21). To facilitate the ability to detect an enhancement of cell expansion, cells were seeded at low (~10%) confluency. CAFs co-culture and CAF CM potently enhanced proliferation in multiple TNBC cell models (**Fig. 1F** and **S2D**). In contrast, while CAFs and CAF CM enhanced viability under doxorubicin treatment, the effect was

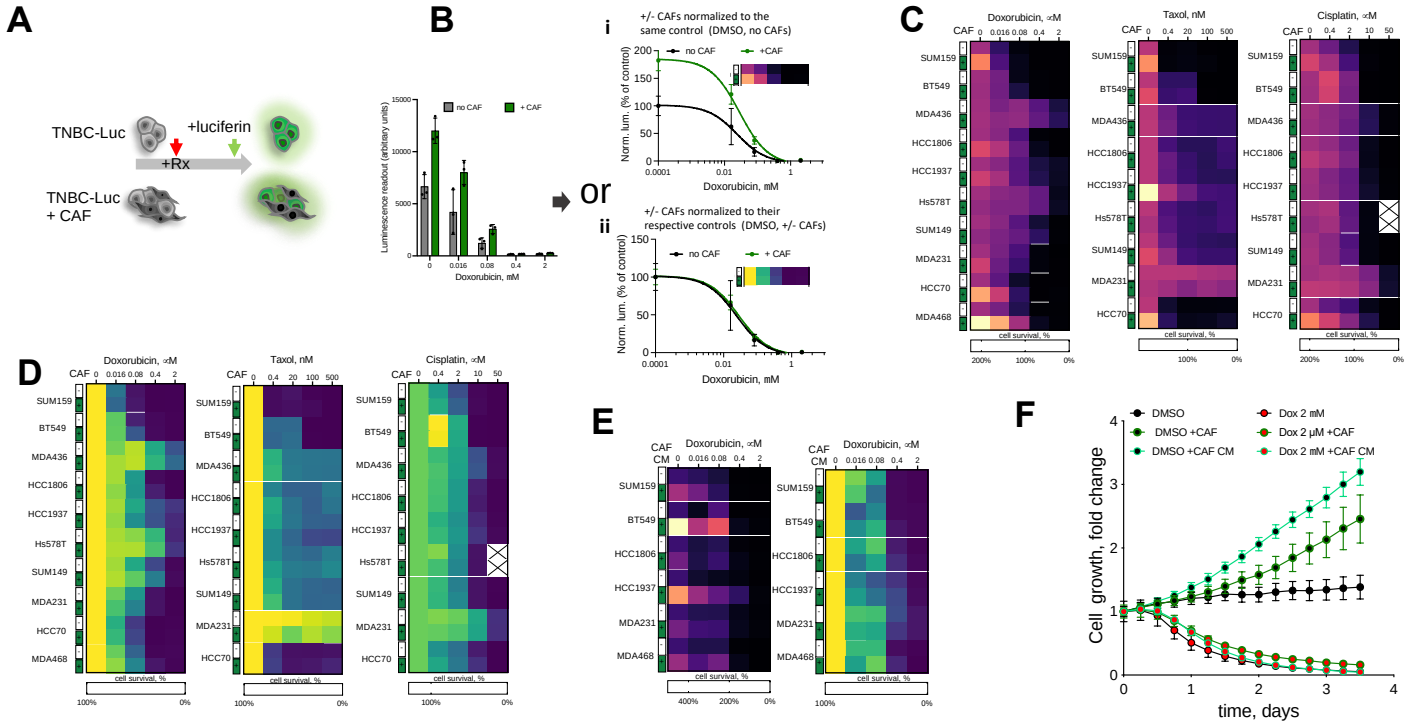

Figure 1. CAFs facilitate TNBC proliferation *in vitro*. A. Experiment diagram for the chemosensitivity viability assay. Luciferase-labeled TNBC cells are cultured in the presence or absence of unlabeled CAFs in the presence of doxorubicin or DMSO vehicle control. Only TNBC cells directly contribute to the viability signal. **B.** Normalization schemata for the data analyses. Raw data from the viability assay can be normalized to either i) the DMSO control signal of cells cultured without CAFs, or ii) with separate normalization of the control and CAF co-cultures to their respective DMSO controls. **C, D.** Heatmap summaries of the impact of CAF co-cultures on doxorubicin sensitivity of a panel of TNBC cell lines, normalized as i) or ii) in panel A respectively. **E.** Heatmap summaries of the impact of CAF CM on doxorubicin sensitivities of the indicated TNBC cell lines. **F.** Impact of CAFs and CAF CM on the growth of GFP-labelled MDA468 cells following 24 hours of doxorubicin exposure, measured by time-lapse microscopy.

much weaker than in the DMSO controls (**Fig. 1F**), suggesting that this enhanced viability reflects a general stimulation of TNBC proliferation.

Proximity to stroma enhances TNBC cell proliferation in experimental tumors.

Next, we sought to assess *in vivo* relevance of our *in vitro* observations. The establishment and growth of experimental tumors in murine models are contingent on the recruitment of host stroma. CAFs play an essential "infrastructural" role by producing ECM that provides the structural organization of tumor tissues, e.g., enabling cell-ECM adhesion and vascularization, *etc*. Therefore, in contrast to *in vitro* studies, a "clean" +/-CAF comparison in experimental tumors is impossible. At the same time, even genetically homogeneous experimental tumors typically display substantial spatial heterogeneity, including regional differences in the stroma-to-tumor ratios. We leveraged this variability by assessing the correlation between stromal content and tumor cell proliferation across semi-randomly selected tumor microdomains of variable tumor tissue across whole tumor cross-sections (**Fig. 2A**). To enable accurate detection of proliferating cells, animals bearing experimental tumors were injected with the dNTP analog BrdU before the euthanasia. Following IHC staining against BrdU, images of whole-slide scans were segmented into micronecrotic regions, stroma, BrdU+ & BrdU- tumor cells using the AI-assisted digital pathology platform Aiforia (https://www.aiforia.com)(**Fig. 2A, S3A**). Consistent with our *in vitro* findings, we found a strong correlation between the fraction of BrdU+ tumor cells and stromal content in MDA468 and BT549 xenograft models of TNBC, under both vehicle control and doxorubicin administration (**Fig. 2B, S3B**).

Encouraged by these observations, we sought to validate these findings with an independent approach that relies on analyses of the distributions of distances between BrdU+ and BrdU- cells and the nearest stroma (**Fig. 2C**). In these analyses, every tumor cell within the tumor cross-section was analyzed, thereby minimizing bias, and improving statistical power. Consistent with the correlation-based analyses, we found a significant difference in the distribution of BrdU+ and BrdU- cells, with BrdU+ cells distributed, on average, closer to the stroma, supporting the notion that stroma-produced paracrine factors stimulate cell proliferation (**Fig. 2D, E**). Importantly, our analyses revealed a similar bias in the distribution of Ki67+ cells in a therapy-naive sample of primary TNBC, suggesting broader relevance to primary human disease (**Fig. 2F, G**).

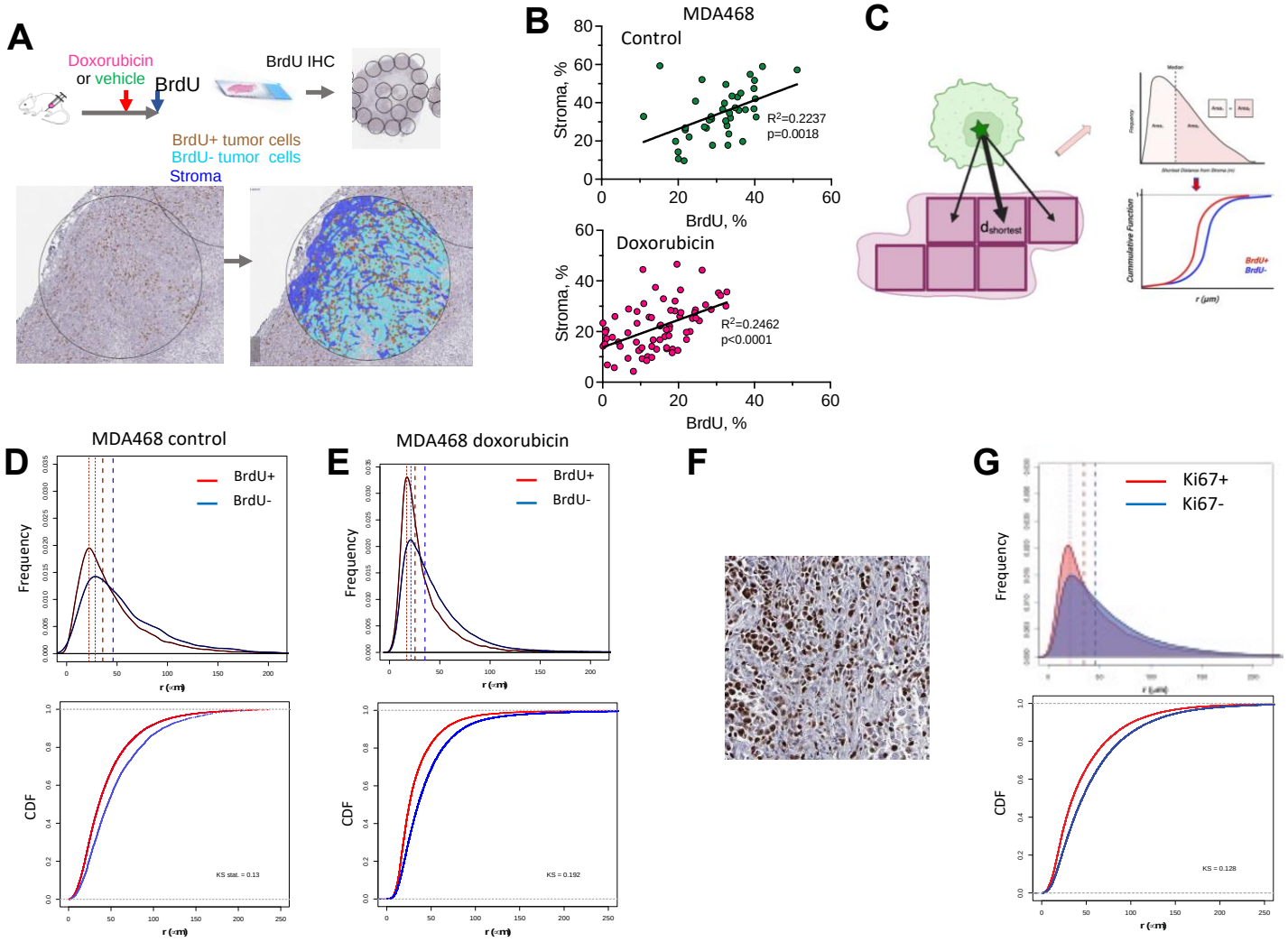

Figure 2. Proximity to stroma correlates with higher proliferation *in vivo.* A. Diagram of the experimental approach to assess the impact of stroma proximity on the proliferation of TNBC cells *in vivo*. Before euthanasia, the mice are pulsed with BrdU, which enables IHC-based detection of cells in the S phase of the cell cycle. Tumor tissue in whole slide scans of BrdU IHC staining is subsampled into smaller areas (0.9 mm in diameter); necrosis-free tumor tissue within these subsampled regions is segmented into BrdU+/- tumor cells and stroma. **B.** Regression analyses of MDA468 xenograft tumors, treated with doxorubicin (2.5 mg/kg) or vehicle control 48 hours before euthanasia assess the correlation between stromal content and tumor cell proliferation. Each dot represents a subsampled area, as in A. R2 and p values of linear regression are shown. **C.** Schemata for the nearest neighbor analyses that calculate distances between each of BrdU+/- cell in the tumor cross-section and the nearest stromal pixel. **D, E.** Frequency distribution and cumulative distribution function (CDF) plots of distances to the nearest stroma of BrdU+/- cells in MDA468 xenografts tumors from control (**D**) and doxorubicin-treated (**E**) mice. Dashed lines indicate medians and means of the distributions. (**E**). **F.** A representative image of a diagnostic biopsy of a therapy-naïve primary human TNBC tumor, stained with proliferation marker Ki67. **G.** Frequency distribution and CDF plots of distances of Ki67+/- cells to the nearest stroma in the primary TNBC sample.

The discovery of a general enhancement of tumor cell proliferation within stroma proximity prompted us to hypothesize an indirect link between stroma and chemoresistance. Cytotoxic therapies, including the ACT regimen used in TNBC therapy, are administered in several cycles of brief chemotherapy exposures separated by several weeks of recovery (22). This pattern administration is based on the well-established concept of a fractional cell kill, *i.e.*, chemotherapy exposure eliminates a fraction of the neoplastic population with each cycle (23), thus necessitating repeated dosing to achieve complete elimination. The length of the recovery between administrations of chemotherapy is typically designed with the aim of minimizing systemic toxicity. Given the short duration of conventional drug administration and the short half-life of chemotherapeutic agents, the surviving tumor cells might partially re-populate the tumor between therapy cycles. Cancer is cured if, over the course of multiple cycles, all of the tumor cells are eliminated or if the surviving fraction is below a threshold for stochastic or immune-mediated extinction. Due to the enhanced proliferation of stroma-proximal cells, tumors with high stromal content could be more likely to avoid therapeutic elimination due to the enhanced ability of residual tumor cell populations to regrow between therapy cycles (**Fig. 3A**).

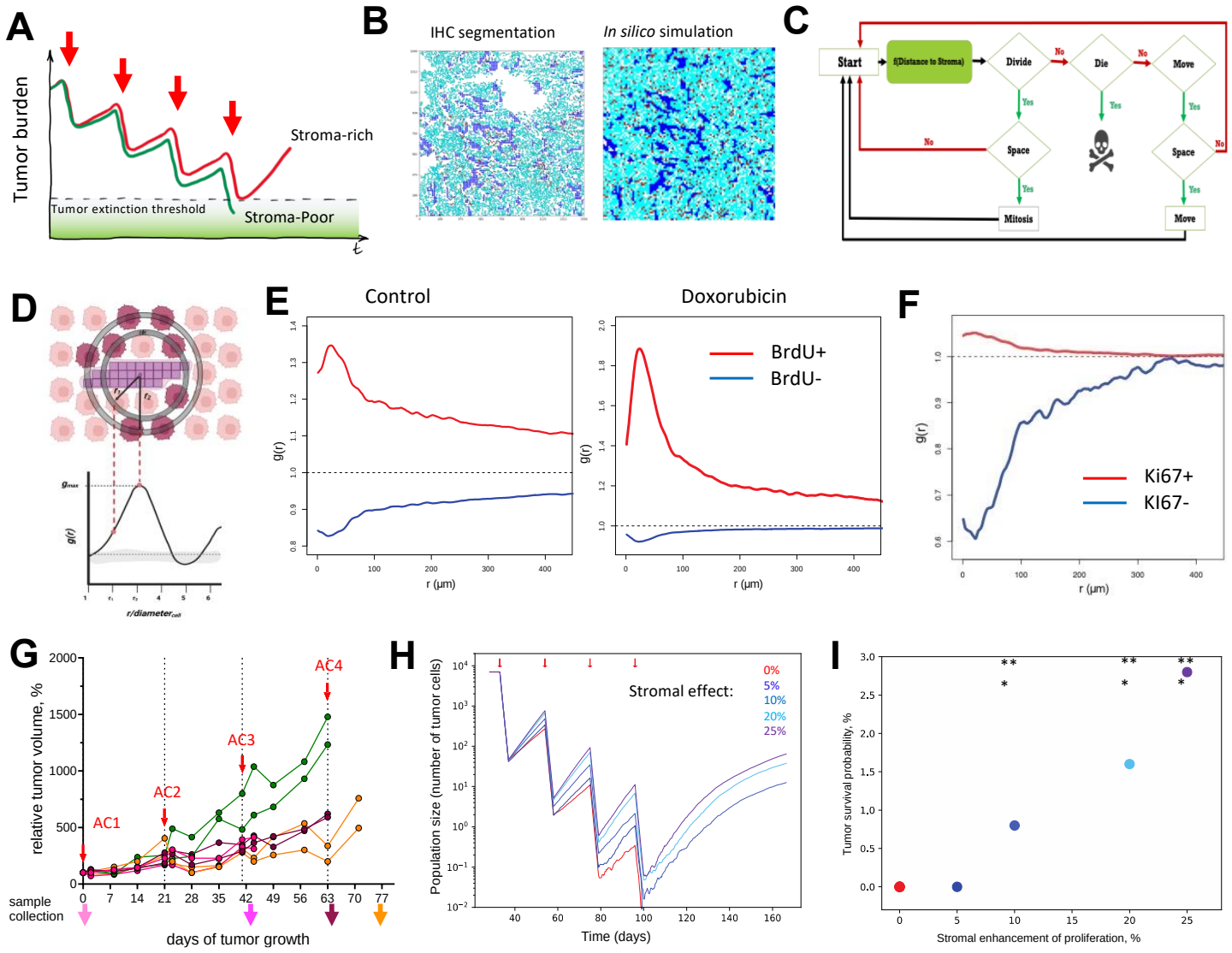

Figure 3. In silico validation of the hypothesized indirect stroma-mediated chemoresistance. A. Model schemata depicting the hypothesized indirect stroma-mediated chemoresistance. Enhanced proliferation in stroma-rich tumors can enhance between-chemo cycles recovery of tumors, enabling them to escape therapeutic eradication. **B.** ABM is initiated based on the spatial localization of tumor cells and stroma observed in the indicated experimental sample. **C.** Diagram of the ABM model. **D.** Schemata for the radial distribution function. **E.** RDF analyses of the impact of stroma proximity on the distribution of BrdU+/- cells in control and doxorubicin-treated MDA468 tumors. **F.** RDF analyses of the impact of stroma proximity on the distribution of Ki67+/- cells in a treatment naïve primary TNBC tumor. **G.** Dynamics of volume changes in MDA468 xenograft tumors over the course of AC treatment (0.5 mg/kg doxorubicin and 50 mg/kg cyclophosphamide), injections times are indicated by red arrows. Traces indicate individual tumors; distinct colors of volume traces indicate tumors harvesting at different time points, indicated by arrows of matching colors. **H**. Impact of the indicated magnitude of enhancement of cell proliferation within 3 cell diameters from stroma border on the average population size over the course of chemotherapy. Traces depict average population sizes over 500 simulations per condition. **I.** Impact of the indicated magnitude of enhancement of cell proliferation on the probability of tumor survival through the course of therapy, over 500 simulations. *** indicates <0.001 p-values of Fisher exact test in comparing the indicated stromal enhancement values to simulations without stromal effect.

To quantitatively capture the impact of stroma on the proliferation of tumor cells, we used the radial distribution function (RDF), **g**(**r**), often used in the field of spatial ecology (24–26). RDF compares the average density of observed BrdU+/- tumor cells against randomly distributed BrdU+/- across different length scales from each of the stromal pixels. The location of the RDF peak, $\mathbf{g_{max}}$, indicates the spatial distance of an effect (such as the stromal impact on proliferation). The value of $\mathbf{g_{max}}$ itself indicates the magnitude of the effect (**Fig. 3D**). To improve the accuracy of our analyses, we analyzed all neoplastic cells within each cross-section. Thus, each analysis captured 10^4 to 10^6 cancer cells per tumor, with multiple tumors analyzed per experimental condition.

The RDF revealed that, in MDA468 murine tumors, the proliferation probability of cells (inferred using BrdU staining) within 2-3 cell diameters from the stromal boundary (~ 30 μM) was increased by 30-40% in the chemotherapy naïve sample, and further increased after doxorubicin treatment (**Fig. 3E**). Next, we applied our analyses to the human sample. In contrast to the BrdU staining, Ki67 is expressed through all active phases of the cell cycle, labeling most cells in actively proliferating tumors. Therefore, the distribution of the less frequent

Ki-67 cells is more informative. RDF distribution of Ki67- cells revealed a 60% increase of cell proliferation within 3 cell diameters from the stroma (**Fig. 3F**). Taken together, our analyses indicate a 30-60% enhancement of cell proliferation in both murine and human tumors within two to three cell diameters distance from the stroma.

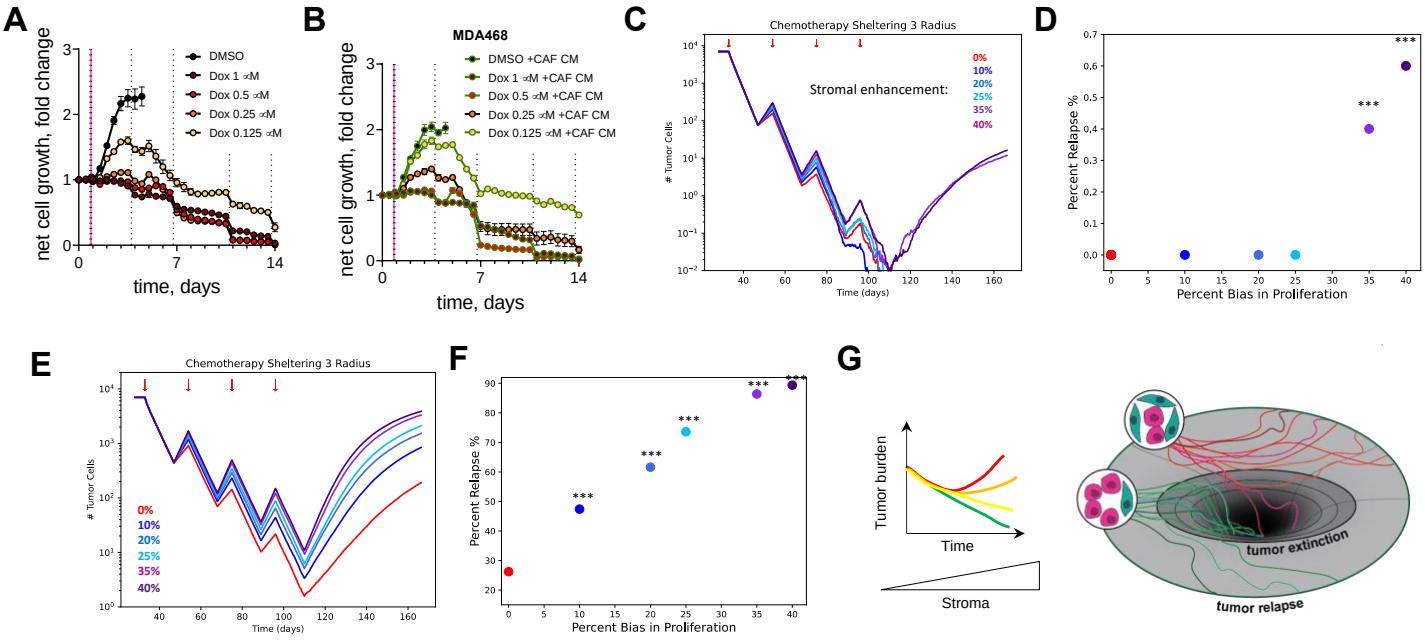

Figure 4. Impact of the stroma- enhanced proliferation on tumor chemotherapy recovery. A, B. Changes in numbers of viable MDA468 cells following brief (2-hours) administration of doxorubicin in control medium (**A**) and with CAF CM (**B**). **C, E.** Impact of the indicated magnitude of enhancement of cell proliferation within 3 cell diameters from stroma border on the average population size over the course of chemotherapy that, in the absence of stromal effects eliminates tumors with 0% (**C**) and 27% (**E**) relapse probability. Traces depict average population sizes over 500 simulations per condition. **D, F.** Impact of the indicated magnitude of enhancement of cell proliferation on the probability of tumor survival through the course of therapy that, in the absence of stromal effects eliminates tumors with 0% (**D**) and 27% (**F**) relapse probability. Graphs depict the outcomes of 500 simulations. *** indicates <0.001 p-values of Fisher exact test in comparing the indicated stromal enhancement values to simulations without stromal effect. **G.** Conceptual model of the indirect stromal chemoresistance. The link between high stromal content and chemoresistance might be at least partially mediated by the stroma-dependent potentiation of tumor cell proliferation, which enhances tumor recovery between chemotherapy cycles and decreases the odds of chemotherapeutic extinction.

The impact of this hypothesized indirect, stroma-mediated chemoresistance towards clinical responses depends on the combined output of proliferation and death of tumor cells during therapy and recovery phases and the magnitude and distance of the stromal impact. Given the lack of direct experimental control over the presence and effects of stroma and the paucity of publicly available experimental animal models of ACT-mediated tumor extinctions, an adequate experimental test for this hypothesis is not feasible. Therefore, we decided to test the relevance of our hypothesis *in silico*, based on the quantitative inferences of relevant parameters derived from our experimental data. To this end, we constructed a spatial on-lattice agent-based model (ABM), using the HAL platform (27). The ABM was initialized as a 100x100 cell grid with an initial location of tumor cells and stromal areas mirroring locations of cells and stroma in histological data (**Fig. 3B)**. Stroma remains static throughout the simulation. In contrast, tumor cells proliferate (if the space is available) and die at rates that match the experimental inferences described above (**Fig. 3C)**.

Enhanced proliferation of stroma-proximal tumor cells can rescue tumors from therapeutic extinction.

To elucidate the impact of multiple therapy cycles on proliferation/death dynamics and the impact of stroma proximity, we subjected a cohort of mice bearing MDA468 xenograft tumors to a clinically relevant regimen of four cycles of AC (doxorubicin/cyclophosphamide) treatment with three-week-intervals between cycles. Tumors were harvested two days after the first, third, and fourth cycles, with additional 2 tumors harvested two weeks after the fourth cycle (**Fig. 3 G**). Similar to the observed responses of MDA468 xenografts to doxorubicin (**Fig. 2C)**, the doxorubicin/cyclophosphamide combination led to a ~ 2-fold reduction in the fraction of BrdU+ cells,

independently of the number of AC cycles. This reduction persisted even after two weeks of recovery (**Fig. S4A**). Treatment only slightly increased the stroma-to-tumor ratio (**Fig. S4B**); no statistically significant increase in the staining for apoptotic marker cleaved caspase 3 could be observed (**Fig. S4C**).

Chemotherapy slowed the growth of MDA468 xenograft tumors, but it failed to induce substantial tumor regression (**Fig. 3 E**). This observation is consistent with the inability of commonly used TNBC models to recapitulate clinical responses to chemotherapy. At the same time, the MDA468 model closely recapitulates the baseline growth and proliferation/death dynamics of primary human tumors (28), as well as the stroma-proximity effect (compare **Fig2D** and **Fig2G**). Therefore, we reasoned that, while our experimental data cannot provide accurate estimates of therapy-induced tumor cell elimination, it enables adequate parameterization for the baseline proliferation/death rates for the *in silico* model. Changes in tumor volume in MDA468 xenograft tumors can provide a reasonably accurate estimate of the net growth rate. However, a given net growth rate can result from highly different birth (proliferation) and death rate combinations. For example, a slow increase in tumor volume can reflect either low proliferation or high cell turnover.

Using the BrdU label in experimental tumors enables accurate quantitation of the fraction of tumor cells in the replication (S) phase of the cell cycle from histological data (29). Given the highly conserved rate of S phase duration in mammalian cells (8-12 hours), the proportion of BrdU+ cells can be used for accurate estimates of tumor birth rates (30). It is impossible to obtain similar direct estimates for tumor death rates from histological data. Still, death rates can be inferred from the discrepancy between the easily measurable net proliferation and birth rates. Following these considerations, we estimated average proliferation rates as ~0.36 per day and average death rates as ~0.3 per day within therapy-naïve tumors. Given the observed reduction in the birth rates after the start of chemotherapy, birth and death rates change to 0.198 and 0.165 per day, respectively (see Supplementary Methods).

Given the lack of strong tumor shrinkage in the xenograft model, experimental data could not be used directly for quantitative estimates of chemotherapy-induced death rates. Therefore, we used the ABM simulation for these estimates. Specifically, we sought to determine the chemotherapy-induced death that, in the absence of stromal effects, is sufficient to completely eliminate in silico tumors over the course of four chemotherapy cycles under the fractional cell kill scenario. Given the short infusion duration and the rapid pharmacokinetics of chemotherapeutic agents *in vivo*(31), the initial drug-induced damage should be inflicted within hours. However, cell death triggered by this damage is not instantaneous. Cell viability assays, commonly used in preclinical *in vitro* studies to evaluate therapeutic sensitivities (such as the MTT assay), involve viability readouts that integrate cytostatic and cytotoxic effects three to four days post-drug administration. Therefore, in our *in silico* simulations, we decided to equally distribute therapy-induced tumor cell death over the course of four days (without directly affecting cell birth rates), then return death rates to the baseline. An example of a simulation run of the model is shown in **video S1**. We found the minimal therapy-induced death rate that is sufficient to eliminate *in silico* tumors with complete penetrance (100% extinction rate in 500 simulations) after four chemotherapy cycles in the absence of stroma proximity to be 0.45 per day (**Fig. S5 A, B**).

Next, we assessed the effect of increased cell proliferation in stroma-proximal niches on the penetrance of therapeutic cures. Even though we observed an increase in proliferation bias within the stroma-proximal niche after chemotherapy administration (compare Figs. **3C** and **S4B**), we decided to use a more conservative estimate of proliferation enhancement by tumor stroma of 40% or less in treatment-naïve tumors. We found that even a 10% enhancement of cell proliferation over 3 cell diameters from the stromal border enabled some tumors to avoid elimination (**Fig. 3 H, G, Video S2**). While only a small fraction of the *in silico* tumors avoided elimination, our simulations contained below 10,000 cells. Therapy failure rate should increase proportionally within larger populations. For example, 1% therapy failure in our simulation would indicate 10% failure in 10 times larger *in silico* tumors.

Next, we sought to perform an experimental proof of principle test of the accelerated recovery hypothesis. Given the lack of options to experimentally control the presence/absence of stroma or its proliferation-enhancing effects *in vivo,* we decided to take advantage of the ability of a “clean” modulation of proliferation-enhancement effects by CAF CM *in vitro*. To recapitulate the short *in vivo* duration of chemotherapy exposure, doxorubicin and other chemotherapy drugs were added to the media for two hours, then the media was replaced after a thorough PBS wash to remove the residual drug. Given the assumption that the surviving cells after the four days of transient drug exposure should be able to recover, we initially focused on doxorubicin concentrations that eliminate the majority of MDA468 cells by four days post-exposure in the absence of CAF CM. Surprisingly, we found that, under these conditions, no viable tumor cells could be recovered with prolonged cultures. Time-lapse

experiments revealed a continuing decline in the numbers of tumor cells, even with lower doxorubicin concentrations where cells initially expanded after the transient drug treatment (**Fig. 4A**).

Notably, the decline in cell numbers occurred despite the active proliferation of tumor cells, consistent with a lasting induction of increased cell death rates (**Video S3**). The effect was not limited to MDA468 cells, as a similar lasting decline in cell numbers was observed in HCC1806 and HCC1937 cell lines despite substantial differences in their doxorubicin sensitivities (**Fig. S6A, B**). Moreover, the lasting increase in tumor cell death extended beyond TNBC cell lines and doxorubicin. The lasting effects of chemotherapy were also observed across a large panel of TNBC cell lines treated with Taxol (data not shown) and in the A678 cell line model of Ewing sarcoma, following exposure to doxorubicin, vincristine, and 4-HU (**Fig. S6C**), suggesting broad generalizability of these results.

The addition of CAF CM partially counteracted the continuing loss in the numbers of MDA468 cells (**Fig. 4B**). Visual examination of the time-lapse video indicated that some of the MDA468 cells survived the therapy in the presence of CAF CM (**Video S4**) at concentrations of doxorubicin that led to complete elimination of control cultures (**Video S3**). Similar effects were observed in the HCC1806 and HCC1937 TNBC models. While these observations do not provide direct proof of the principle of the accelerated recovery hypothesis, they support the notion that proliferation-enhancing effects of paracrine signals produced by stroma can reduce chemotherapy efficiency.

The extended duration of the cytotoxic effects of the chemotherapeutic agents should reduce the time available for the recovery of the residual cancer cell populations. Therefore, we used the ABM simulation approach to evaluate whether the proliferation-enhancing effects of stroma can still enhance chemoresistance when the therapy-induced increase in cell death extends beyond four days. The fitting of *in vitro* experimental data indicated that chemotherapy induces a monotonous decrease in cancer cell numbers rather than a bi-phasic response, where a high initial cell kill is followed by lower-intensity lingering effects (**Fig. S6A** & Mathematical Supplement). While the HCC1937 and A673 cell lines transitioned to net positive cell growth one week after chemotherapy exposure (**Fig. S5B, C**), we decided to use a more conservative two-week estimate of the duration of chemotherapy based on MDA468 data, leaving one week for recovery.

We used the ABM to find the kill rate that would lead to the complete elimination of *in silico* tumors and then asked whether the observed proliferation enhancement rates could enable the tumors to avoid elimination. As expected, the extended duration of chemotherapy-induced cell death translated into a reduction in death rates, necessary to eliminate the tumors over the course of four cycles of chemotherapy from 0.45/day (**Fig. S4E, F,** to 0.2/day (**Fig. S6B, C**). The ability of stroma to rescue tumors from therapeutic extinction was also reduced, but not entirely negated, as tumor recovery was only observed under proliferation-enhancement rates of over 35%, and the penetrance of therapy rescue was lower (**Fig. 4C, D**), compared to the four-day duration of therapy-induced cell kill (**Fig. 3 H, I**).

Next, we evaluated the impact of stroma under a scenario of partial penetrance of therapy-induced tumor extinction, with ~25% relapse probability observed under the therapy-induced cell death of 17% per day. Under this scenario, even a 10% enhancement of proliferation within 3 cell distances from the stroma almost doubled the relapse probability (**Fig. 4E, F**). The effect was even more pronounced with the stronger stromal enhancement (**Fig. 4E, F**). Therefore, even in the absence of a specific reduction in chemosensitivity, a general enhancement of tumor cell proliferation in stroma-proximal niches can enable tumors to escape elimination during the course of chemotherapy (**Fig. 3A and 4G**). This mechanism is not mutually exclusive with the simultaneous action of other mechanisms of chemoresistance, including cell-intrinsic differences in drug sensitivity, dormancy, or direct cytoprotectant by stromal paracrine signals. Overall, our results suggest the existence of a new, indirect chemoresistance mechanism of accelerated residual tumor recovery, which might contribute to the known link between high stromal content and poor outcomes.

Discussion.

Despite the advances in basic and clinical cancer research, the combination of surgery and chemotherapy usually fails to eradicate advanced cancers, including TNBC. Improving clinical outcomes requires an accurate and comprehensive understanding of the biological mechanisms that enable tumors to avoid therapeutic elimination. Whereas tumor responses to therapies are primarily shaped by the cell-intrinsic properties of tumor cells, this does not exclude the contribution of additional factors. The strong correlation between high stromal

content, chemoresistance, and poor patient survival (9) suggests a role for microenvironmental modulators of chemoresistance. In the context of targeted therapies, paracrine factors, including elements of the ECM and cytokines produced by CAFs and other non-neoplastic cells within the TME, can strongly desensitize cells to targeted inhibitors by activating alternative signaling pathways (32–34). A similar link has been reported in the context of chemotherapy (35,36). However, the magnitude of the direct effects of stroma on chemosensitivity appears to be much lower, and the generalizability of these effects is far less clear, as modulation of cell signaling is less capable of impacting the cellular damage created by chemotherapy. Our studies uncover a novel mechanism of stroma-mediated chemoresistance that does not involve direct chemoprotection. Instead, treatment-independent enhancement of tumor cell proliferation in the stroma's vicinity can augment residual tumors' ability to recover between chemotherapy cycles, decreasing the odds of therapeutic extinction over the course of treatment (**Figs. 3A & 4G**). Notably, while our study does not explicitly address it, the relevance of the accelerated recovery mechanism is likely not limited to the impact of the stroma. Accelerated recovery in between chemotherapy cycles might be contributing to the link between a high proliferative index and poor outcomes, independently of the mechanisms responsible for the enhanced proliferation, such as poor outcomes in Ewing sarcomas, which are relatively stroma-poor (37). We see clear parallels with r/K reproductive strategies in evolutionary ecology (38). Cell-intrinsic and cell-extrinsic mechanisms involving direct protection against the cytotoxic and cytostatic effects of the drugs are analogous to the K strategy, focused on enhanced protection/survival. In contrast, the indirect protection mechanism suggested by our study is analogous to the r strategy, where reproductive success is achieved by maximizing the number of offspring.

Since the discovery of the genetic underpinnings of cancer, the identification of the molecular mechanisms that underlie their responses to existing therapies and the search for new molecular targets have become the main focus of basic cancer research. Standard research pipelines often include assays that measure the response of cancer cells to a range of drug concentrations, typically measured at a single time point 3-4 days after the start of the treatment. These assays quantify the number of viable cells (via proxy readouts, such as MTT), relative to the number of cells in vehicle-treated control. The results are commonly expressed as drug concentrations that lead to a two-fold reduction in viability signal (LD50, or ID50). The universal use of these assays indicates an implicit assumption that a single temporary snapshot of cell viability is sufficient to predict the overall drug efficiency. This approach does not discriminate between cytotoxic and cytostatic effects and leads to some apparent paradoxes. For example, TNBC or Ewing sarcoma cells tend to be highly sensitive to standard-of-care chemotherapies, yet these tumors are highly resistant to therapeutic elimination. This discrepancy is often attributed to intratumor heterogeneity or dormancy, i.e., some tumor cells avoid elimination either due to drug insensitivity or the ability to “sleep through the storm” through quiescence. Whereas this attribution is based on solid experimental and clinical evidence, even in the absence of ITH or dormancy, the success or failure of a course of chemotherapy in eliminating neoplastic populations is strongly influenced by other factors. For the standard chemotherapies, administered as cycles of acute drug exposure separated by two to three weeks, the outcome reflects the net outcome of proliferation and death dynamics of neoplastic populations throughout the course of the treatment.

Identical short-term cell viability readouts can hide vastly different longer-term outcomes. For example, a longer duration of the acute cytotoxic/cytostatic effects increases therapy efficiency by enhancing fractional cell kill and reducing the time available for the residual tumor to recover. Perhaps less obvious, but equally important is that the net change in the number of cells, measured by cell viability assays *in vitro*, or volumetric/biomarker/bioluminescence measurements *in vivo*, reflects a balance between proliferation and death of tumor cells. Even when measured through multiple time points, identical baseline net growth rates can hide highly different rates of cell turnover, with significant consequences for the ability of tumors to recover from treatment, or for the speed of competitive expansion of resistant subpopulations. These considerations are typically neglected when interpreting experimental data or designing clinical therapies.

Apart from recognizing the importance of proliferation/death rates, addressing this gap requires the development of robust approaches to measure the critical parameters of cell population dynamics. In contrast to the vast advances in techniques for molecular analyses, very little progress has been made in approaches to infer proliferation/death rates in space and time. Moreover, even if accurate measurements of these rates were readily available, it is not always possible to assess their contribution to biologically or clinically relevant outcomes through standard tools. For example, it is not intuitively clear how a 10-20% difference in the birth rate of cancer cells within 3 cell diameters from stroma (as reflected in the fraction of BrdU+ cells) would impact the fraction of tumor cells that escape elimination over multiple cycles of treatment. The lack of linearity and the need to integrate the impact of multiple parameters limits the utility of standard statistical inferences, instead necessitating the need to use appropriate biologically driven and parameterized mathematical modeling tools.

The incorporation of proliferation/death dynamics could enable a substantial improvement in clinical outcomes. For example, blocking the slight enhancement of proliferation in the vicinity of stroma might lead to a several-fold increase in the odds of tumor elimination (**Fig4, E, F**). However, the feasibility of this strategy in clinical applications depends on identifying the underlying molecular mechanisms and on the feasibility of their therapeutic modulation. Given the substantial biological diversity of TNBC, the relationship between stromal proximity and tumor cell proliferation might vary between tumors. Stroma is a heterogeneous compartment, and the effects of stroma proximity might vary even within individual tumors. Importantly, even in cases where enhancement of proliferation contributes to the ability of tumors to survive therapy, this does not exclude the essential importance of additional mechanisms, such as intrinsic chemotherapy resistance due to cancer dormancy.

In summary, our study proposes a novel indirect chemoresistance mechanism where stroma-rich tumors are more likely to avoid therapeutic eradication by accelerating residual tumor recovery between chemotherapy cycles (**Figs. 3A and 4G**). We provide proof of principle validation of this mechanism under realistic birth/death dynamics. While further work is needed to characterize the contribution of this mechanism to chemoresistance in clinics, these findings implicate new opportunities for therapeutic interventions. Further, our study highlights the limitations of standard viability assays to understand the impacts of therapies. Our work points to the utility of understanding the spatiotemporal birth/death dynamics of cancer cells through the integration of experimental and mathematical modeling.

Methods.

IHC staining. Formalin-fixed, paraffin-embedded tumors were cut at 5 microns sections. Deparaffinized tissue slices were blocked in PBS with 10% goat serum for 30 min at room temperature, then incubated at room temperature for 1 hour with primary anti-BrdU antibodies (1:100, Sigma#11170376001) and 1 hour with secondary antibodies (1:100, Vector Labs BA-9200), with 3x10 min washes after each incubation. The staining was developed using Vectastain ABC HRP Kit (Vector Labs, PK-6100), following manufacturer's protocol. Cytoseal XYL mounting media (Epredia) was used to mount the slides.

Histology image segmentation. IHC images were scanned with Aperio ScanScope XT Slide Scanner (Leica). The image areas corresponding to tumor tissue were segmented into BrdU+/- tumor cells, stroma, and necrotic tissue, with necrotic tissue excluded from the analyses (**Fig. S3A**). The segmentation was performed using an artificial intelligence (AI) based semi-automated deep learning quantification method (Aiforia version 5.2, Aiforia Inc, Cambridge, MA). Our training set for segmentation consisted of 20 slides, including samples after treatment and before treatment. An artificial intelligence-based software (Aiforia) was trained to recognize the nuclei of proliferating (stained with the proliferation marker BrdU) and non-proliferating tumor cells and record the x-y coordinates of the center of the nuclei. The stromal areas were segmented as polygons without separating cellular and ECM components. Segmentation accuracy was examined and approved by American Board of Pathology certified pathologist. Segmentation was performed on selected ROI for the initial correlation analyses. For proximity to the nearest stroma and RDS analyses, all of the tumor tissue was subjected to segmentation. Segmentation masks were downloaded as rds. Files for downstream analyses.

Spatial statistics analyses. For the correlation analyses between the fraction of BrdU+ cells and stromal content, ROIs of 0.9 mm diameter were semi-randomly sampled from the tumor tissue area, avoiding large necrotic areas. Each ROI was segmented using the Aiforia AI model described above. The stromal area was calculated as a fraction of the ROI area, excluding necrotic tissue. The correlation between stroma and BrdU+ cells was calculated in GraphPad Prism using the simple linear regression method.

Advanced spatial statistics analyses were performed using R 4.1.2. The point pattern extraction from the Aiforia-segmented images has been performed using a combination of "sf" and "Magick" packages. Spatial statistics analyses were performed using the "Spatstat ", "kSamples", "sp" and "Goftest") packages. Polygonal segmentation of tumor stroma was tiled/pixelated using R package "sf" and "magick" into squares with the length of an average tumor cell diameter (15 μm). X-y coordinates of the center of each square (stroma unit/pixel) were recorded and used for the subsequent analyses.

For the analyses of distances to the nearest stroma, for each marker positive and marker negative (BrdU or Ki67) tumor cell, the Euclidian distance to the nearest stroma pixel was determined, and the distance frequencies and cumulative density graphs were plotted. Cumulative density functions of the respective distributions were

used for analyses of the statistical significance of differences between distances of marker positive and marker negative cells by the Kolgomorov-Smirnoff test.

The RDF compares the average density of points against complete spatial randomness (CSR) across different length scales. To calculate the RDF for the distribution of marker positive/negative cells relative to the stroma, an annulus of width *dr* and radius *r* is placed around each of the stroma pixels. The number of marker +/- tumor cell centers within each annulus was calculated and divided by the expected number of tumor cell centers that fall inside the annulus under CSR. This calculation was repeated for each of the stromal pixels, and then the average value over all points at a certain *r* was recorded. CSR was generated *in silico* by maintaining the position of tumor cells and stromal pixels, as well as numbers of marker positive/negative tumor cells, but randomly shuffling tumor cell labels (marker status). For each sample, we generated a series of 39 CSF distributions and calculated a CSR average and 95% envelope of confidence.

Agent-Based Modeling. The on-lattice ABM was developed using the Hybrid Automata Library (HAL) Java Library platform (27). In our model, cells are positioned in a 100 cells x 100 cells grid; the initial distribution of tumor cells and stroma is based on the Aiforia-extracted mask of an IHC slide image representing 1500 μm x 1500 μm area. Each cell on the grid can be occupied by a tumor cell, stroma or be empty. Tumor cells are represented by agents that can divide, die, and move, while stromal pixels remain static. Time is discrete, with each time step representing 8 hours. At any timestep, the tumor cells can divide if there is an empty grid space in their immediate vicinity, die, or move to an available grid point in their vicinity (see **Fig. 3G**). The probability of proliferation is conditioned by the proximity to the stroma, with the effect extending to tumor cells within 3 cells from the stromal pixels. Parameter values are described in **Table S1**. Details on the model and derivation of parameters from experimental data are provided in the Supplementary Methods.

Cell lines and tissue culture conditions. Breast cancer cell lines were obtained from the following sources: MDA-MB-231, HCC1937, HCC1806, BT549, MDA-MB-436, HCC70, HS578T from ATCC and SUM149PT from Dr. S. Ethier (University of Michigan, Ann Arbor, MI). Breast cancer and normal fibroblasts were isolated from patient samples as previously described using protocols approved by the Dana-Farber Harvard Cancer Center (DF/HCC) Institutional Review Board. Fibroblast and SUM149PT cells were cultured in 50/50 mixture of DMEM-F12/MEGM with supplements containing 5% FBS; all other cell lines were cultured in in ATCC-recommended media. Cell line identities were confirmed by STR analysis. All cell lines and CAF isolates were routinely tested for mycoplasma contamination.
Luciferase expressing derivates of TNBC cell lines were obtained as described in (20). Fluorescently labelled cells for time-lapse microscopy studies were derived from the corresponding cell lines using a custom lentiviral vector which provides a nuclear expression of mCherry or GFP, coupled with puromycin expression, as described in (21). CAF-conditioned media was collected from confluent 10 cm dishes of CAFs grown in the fibroblast media. CAF CM experiments were performed in 50/50 mixtures of cell line-specific media with either CAF CM or fibroblast media.

Cell viability readouts. For the luminescence-based readouts, firefly luciferase-expressing cells were grown in clear bottom white opaque 96 well plates (Corning, 3610). 30 min before taking the reading, the medium was replaced with fresh medium containing 25 µg/ml d-luciferin (GoldBio LUCK-2G). The luminescence signal was determined using GloMax luminometer (Promega); the background from the cell-free wells was subtracted from each reading. For microscopy-based readouts, time-lapse videos were generated with IncuCyte live cell imaging system (Sartorius) using ZOOM 4x objective. Images were acquired in red and green fluorescent channels as well as visible light channel every 12 hours for 7-21 days. Propidium iodide was added to the culture medium at 0.5 µg/ml to label dead cells. For the viability assays focused on assessing therapy responses, cells were seeded at 3.5×10^4 cells per well to achieve ~80% initial confluency. For the proliferation assays assessing the impact of CAFs and CAF CM on cell growth in the absence of treatment, cells were seeded at 3×10^3 to achieve ~5% initial confluency. For the fibroblast co-culture experiments, cells were plated in 3:1 TNBC: CAF ratios in 96 well-clear bottom tissue culture plates (Falcon #353072).

Mouse xenograft studies
Tumors were initiated by orthotopic injection of 8 weeks old female NSG mice 1×10^6 cells, suspended in 50/50 mix of DMEME-F12 culture media and Matrigel (BD Biosciences), in 100 µl volume; each animal was implanted

with two tumors on the opposite flanks. Tumor growth was monitored weekly by electronic caliper measurements as described in (Vander Velde et al., 2020). 30-40 min prior to euthanasia, mice were injected with 10 mg/ml BrdU dissolved in PBS. Tumors were fixed in formaldehyde and embedded in paraffin. All animal experiments were performed in accordance with the approved procedures of the IACUC protocol #IS00005557 of the H. Lee Moffitt Cancer Center.

Statistical analyses

Statistical analyses of *in vitro* and *in vivo* experimental data were performed using GraphPad Prism software, using statistical tests indicated in figure legends. Statistical analyses for the *in silico* simulations were performed with R and MatLab.

Acknowledgments:

This project is supported by the Florida Breast Cancer Foundation (A. Marusyk and D. Basanta), Moffitt Cancer Center Evolutionary Therapy Center of Excellence (A. Marusyk, D. Basanta and P.A. Altrock), William G. 'Bill' Bankhead Jr and David Coley Cancer Research Program 20B06 (A. Marusyk, D. Basanta and P.A. Altrock); S. G. Komen Research & Training grant (A. Marusyk), Richard O. Jacobson Foundation (P.A. Altrock). This work has been supported in part by the Analytic Microscopy Core, Vivarium Core and the Tissue Core at the H. Lee Moffitt Cancer Center & Research Institute, a comprehensive cancer center designated by the National Cancer Institute and funded in part by Moffitt's Cancer Center Support Grant (P30-CA076292). We would like to thank Jacob Scott and Bina Desai for their thoughtful comments and suggestions.

References:

1. Ge W, Yue M, Wang Y, Wang Y, Xue S, Shentu D, et al. A Novel Molecular Signature of Cancer-Associated Fibroblasts Predicts Prognosis and Immunotherapy Response in Pancreatic Cancer. Int J Mol Sci [Internet]. 2022 Dec 21 [cited 2023 Jan 12];24(1):156. Available from: https://pubmed.ncbi.nlm.nih.gov/36613599/
2. Xu J, Fang Y, Chen K, Li S, Tang S, Ren Y, et al. Single-Cell RNA Sequencing Reveals the Tissue Architecture in Human High-Grade Serous Ovarian Cancer. Clinical Cancer Research [Internet]. 2022 Aug 15 [cited 2023 Jan 12];28(16):3590–602. Available from: https://aacrjournals.org/clincancerres/article/28/16/3590/707396/Single-Cell-RNA-Sequencing-Reveals-the-Tissue
3. Irvine AF, Waise S, Green EW, Stuart B, Thomas GJ. Characterising cancer-associated fibroblast heterogeneity in non-small cell lung cancer: a systematic review and meta-analysis. Scientific Reports 2021 11:1 [Internet]. 2021 Feb 12 [cited 2023 Jan 12];11(1):1–15. Available from: https://www.nature.com/articles/s41598-021-81796-2
4. Jamieson NB, Carter CR, McKay CJ, Oien KA. Tissue biomarkers for prognosis in pancreatic ductal adenocarcinoma: a systematic review and meta-analysis. Clin Cancer Res [Internet]. 2011 May 15 [cited 2023 Jan 12];17(10):3316–31. Available from: https://pubmed.ncbi.nlm.nih.gov/21444679/
5. Graizel D, Zlotogorski-Hurvitz A, Tsesis I, Rosen E, Kedem R, Vered M. Oral cancer-associated fibroblasts predict poor survival: Systematic review and meta-analysis. Oral Dis [Internet]. 2020 May 1 [cited 2023 Jan 12];26(4):733–44. Available from: https://pubmed.ncbi.nlm.nih.gov/31179584/
6. Hu H, Piotrowska Z, Hare PJ, Chen H, Mulvey HE, Mayfield A, et al. Three subtypes of lung cancer fibroblasts define distinct therapeutic paradigms. Cancer Cell [Internet]. 2021 Nov 8 [cited 2023 Jan 12];39(11):1531-1547.e10. Available from: https://pubmed.ncbi.nlm.nih.gov/34624218/
7. Kramer CJH, Vangangelt KMH, van Pelt GW, Dekker TJA, Tollenaar RAEM, Mesker WE. The prognostic value of tumour-stroma ratio in primary breast cancer with special attention to triple-negative tumours: a review. Breast Cancer Res Treat [Internet]. 2019 Jan 15 [cited 2023 Jan 8];173(1):55–64. Available from: https://pubmed.ncbi.nlm.nih.gov/30302588/
8. Paraiso KHT, Smalley KSM. Fibroblast-mediated drug resistance in cancer. Biochem Pharmacol. 2013 Apr;85(8):1033–41.
9. Farmer P, Bonnefoi H, Anderle P, Cameron D, Wirapati P, Becette V, et al. A stroma-related gene signature predicts resistance to neoadjuvant chemotherapy in breast cancer. Nat Med [Internet]. 2009 Jan [cited 2023 Jan 8];15(1):68–74. Available from: https://pubmed.ncbi.nlm.nih.gov/19122658/
10. Cleator S, Heller W, Coombes RC. Triple-negative breast cancer: therapeutic options. Lancet Oncol [Internet]. 2007 Mar [cited 2023 Jan 8];8(3):235–44. Available from: https://pubmed.ncbi.nlm.nih.gov/17329194/
11. Echeverria G v., Ge Z, Seth S, Zhang X, Jeter-Jones S, Zhou X, et al. Resistance to neoadjuvant chemotherapy in triple-negative breast cancer mediated by a reversible drug-tolerant state. Sci Transl Med [Internet]. 2019 Apr 17 [cited 2023 Jan 8];11(488). Available from: https://pubmed.ncbi.nlm.nih.gov/30996079/
12. Vangangelt KMH, Green AR, Heemskerk IMF, Cohen D, van Pelt GW, Sobral-Leite M, et al. The prognostic value of the tumor-stroma ratio is most discriminative in patients with grade III or triple-negative breast cancer. Int J Cancer. 2020 Apr 15;146(8):2296–304.
13. Loh JJ, Li TW, Zhou L, Wong TL, Liu X, Ma VWS, et al. FSTL1 secreted by activated fibroblasts promotes hepatocellular carcinoma metastasis and stemness. Cancer Res [Internet]. 2021 Nov 15 [cited 2023 Jan 12];81(22):5692–705. Available from: https://aacrjournals.org/cancerres/article/81/22/5692/670494/FSTL1-Secreted-by-Activated-Fibroblasts-Promotes

14. Timperi E, Gueguen P, Molgora M, Magagna I, Kieffer Y, Lopez-Lastra S, et al. Lipid-Associated Macrophages Are Induced by Cancer-Associated Fibroblasts and Mediate Immune Suppression in Breast Cancer. Cancer Res [Internet]. 2022 Sep 15 [cited 2023 Jan 12];82(18):3291–306. Available from: https://aacrjournals.org/cancerres/article/82/18/3291/709018/Lipid-Associated-Macrophages-Are-Induced-by-Cancer
15. Raghavan KS, Francescone R, Franco-Barraza J, Gardiner JC, Vendramini-Costa DB, Luong T, et al. NetrinG1+ Cancer-Associated Fibroblasts Generate Unique Extracellular Vesicles that Support the Survival of Pancreatic Cancer Cells Under Nutritional Stress. Cancer Research Communications [Internet]. 2022 Sep 2 [cited 2023 Jan 12];2(9):1017–36. Available from: https://aacrjournals.org/cancerrescommun/article/2/9/1017/709220/NetrinG1-Cancer-Associated-Fibroblasts-Generate
16. Rosen S, Brisson BK, Durham AC, Munroe CM, McNeill CJ, Stefanovski D, et al. Intratumoral collagen signatures predict clinical outcomes in feline mammary carcinoma. PLoS One [Internet]. 2020 Aug 1 [cited 2023 Jan 12];15(8). Available from: https://pubmed.ncbi.nlm.nih.gov/32776970/
17. Győrffy B. Survival analysis across the entire transcriptome identifies biomarkers with the highest prognostic power in breast cancer. Comput Struct Biotechnol J. 2021 Jan 1;19:4101–9.
18. Ham IH, Lee D, Hur H. Cancer-Associated Fibroblast-Induced Resistance to Chemotherapy and Radiotherapy in Gastrointestinal Cancers. Cancers (Basel) [Internet]. 2021 Mar 1 [cited 2023 Jan 10];13(5):1–17. Available from: /pmc/articles/PMC7963167/
19. Hu Y, Yan C, Mu L, Huang K, Li X, Tao D, et al. Fibroblast-Derived Exosomes Contribute to Chemoresistance through Priming Cancer Stem Cells in Colorectal Cancer. PLoS One [Internet]. 2015 May 4 [cited 2023 Jan 10];10(5). Available from: /pmc/articles/PMC4418721/
20. Marusyk A, Tabassum DP, Janiszewska M, Place AE, Trinh A, Rozhok AI, et al. Spatial Proximity to Fibroblasts Impacts Molecular Features and Therapeutic Sensitivity of Breast Cancer Cells Influencing Clinical Outcomes. Cancer Res [Internet]. 2016 Nov 15 [cited 2023 Jan 10];76(22):6495–506. Available from: https://pubmed.ncbi.nlm.nih.gov/27671678/
21. Miroshnychenko D, Baratchart E, Ferrall-Fairbanks MC, Velde R vander, Laurie MA, Bui MM, et al. Spontaneous cell fusions as a mechanism of parasexual recombination in tumour cell populations. Nat Ecol Evol [Internet]. 2021 Mar 1 [cited 2023 Jan 10];5(3):379–91. Available from: https://pubmed.ncbi.nlm.nih.gov/33462489/
22. Martín M, Seguí MA, Antón A, Ruiz A, Ramos M, Adrover E, et al. Adjuvant Docetaxel for High-Risk, Node-Negative Breast Cancer. New England Journal of Medicine [Internet]. 2010 Dec 2 [cited 2023 Jan 12];363(23):2200–10. Available from: https://www.nejm.org/doi/full/10.1056/nejmoa0910320
23. Chabner BA, Longo DL. Cancer Chemotherapy and Biotherapy: Principles and Practice (Chabner, Cancer Chemotherapy and Biotherapy). 5th ed. Lippincott Williams & Wilkins Next page; 2011. 1–812 p.
24. Law R, Illian J, Burslem DFRP, Gratzer G, Gunatilleke CVS, Gunatilleke IAUN. Ecological information from spatial patterns of plants: insights from point process theory. Journal of Ecology. 2009 Jul;97(4):616–28.
25. Bull JA, Macklin PS, Quaiser T, Braun F, Waters SL, Pugh CW, et al. Combining multiple spatial statistics enhances the description of immune cell localisation within tumours. Sci Rep. 2020 Oct 29;10(1):18624.
26. Younge K, Johnston B, Christenson C, Bohara A, Jacobson J, Butler NM, et al. The use of radial distribution and pair-correlation functions to analyze and describe biological aggregations. Limnol Oceanogr Methods. 2006 Nov;4(10):382–91.
27. Bravo RR, Baratchart E, West J, Schenck RO, Miller AK, Gallaher J, et al. Hybrid Automata Library: A flexible platform for hybrid modeling with real-time visualization. PLoS Comput Biol [Internet]. 2020 [cited 2023 Jan 12];16(3):e1007635. Available from: https://journals.plos.org/ploscompbiol/article?id=10.1371/journal.pcbi.1007635
28. Gurnani M, Lipari P, Dell J, Shi B, Nielsen LL. Adenovirus-mediated p53 gene therapy has greater efficacy when combined with chemotherapy against human head and neck, ovarian, prostate, and breast

cancer. Cancer Chemother Pharmacol [Internet]. 1999 [cited 2023 Jan 10];44(2):143–51. Available from: https://pubmed.ncbi.nlm.nih.gov/10412949/
29. Nowakowski RS, Lewin SB, Miller MW. Bromodeoxyuridine immunohistochemical determination of the lengths of the cell cycle and the DNA-synthetic phase for an anatomically defined population. J Neurocytol [Internet]. 1989 Jun [cited 2023 Jan 10];18(3):311–8. Available from: https://pubmed.ncbi.nlm.nih.gov/2746304/
30. Gerlee P, Altrock PM. Extinction rates in tumour public goods games. J R Soc Interface [Internet]. 2017 Sep 1 [cited 2023 Jan 10];14(134). Available from: https://pubmed.ncbi.nlm.nih.gov/28954847/
31. Mross K, Maessen P, van der Vijgh WJ, Gall H, Boven E, Pinedo HM. Pharmacokinetics and metabolism of epidoxorubicin and doxorubicin in humans. Journal of Clinical Oncology. 1988 Mar;6(3):517–26.
32. Ishibashi M, Neri S, Hashimoto H, Miyashita T, Yoshida T, Nakamura Y, et al. CD200-positive cancer associated fibroblasts augment the sensitivity of Epidermal Growth Factor Receptor mutation-positive lung adenocarcinomas to EGFR Tyrosine kinase inhibitors. Scientific Reports 2017 7:1 [Internet]. 2017 Apr 21 [cited 2023 Jan 10];7(1):1–13. Available from: https://www.nature.com/articles/srep46662
33. Giannoni E, Bianchini F, Masieri L, Serni S, Torre E, Calorini L, et al. Reciprocal activation of prostate cancer cells and cancer-associated fibroblasts stimulates epithelial-mesenchymal transition and cancer stemness. Cancer Res [Internet]. 2010 Sep 1 [cited 2023 Jan 10];70(17):6945–56. Available from: https://aacrjournals.org/cancerres/article/70/17/6945/559773/Reciprocal-Activation-of-Prostate-Cancer-Cells-and
34. Wang W, Li Q, Yamada T, Matsumoto K, Matsumoto I, Oda M, et al. Crosstalk to stromal fibroblasts induces resistance of lung cancer to epidermal growth factor receptor tyrosine kinase inhibitors. Clinical Cancer Research [Internet]. 2009 Nov 1 [cited 2023 Jan 10];15(21):6630–8. Available from: https://aacrjournals.org/clincancerres/article/15/21/6630/75028/Crosstalk-to-Stromal-Fibroblasts-Induces
35. Hisamitsu S, Miyashita T, Hashimoto H, Neri S, Sugano M, Nakamura H, et al. Interaction between cancer cells and cancer-associated fibroblasts after cisplatin treatment promotes cancer cell regrowth. Hum Cell [Internet]. 2019 Oct 1 [cited 2023 Jan 10];32(4):453–64. Available from: https://link.springer.com/article/10.1007/s13577-019-00275-z
36. Ishii T, Suzuki A, Kuwata T, Hisamitsu S, Hashimoto H, Ohara Y, et al. Drug-exposed cancer-associated fibroblasts facilitate gastric cancer cell progression following chemotherapy. Gastric Cancer [Internet]. 2021 Jul 1 [cited 2023 Jan 10];24(4):810–22. Available from: https://link.springer.com/article/10.1007/s10120-021-01174-9
37. Tu J, Huo Z, Gingold J, Zhao R, Shen J, Lee DF. The Histogenesis of Ewing Sarcoma. Cancer Rep Rev [Internet]. 2017 [cited 2023 Jan 31];1(2). Available from: /pmc/articles/PMC5472389/
38. William D. Bowman SDH. Ecology. 5th ed. Sinauer Associates; 2020.
39. vander Velde R, Yoon N, Marusyk V, Durmaz A, Dhawan A, Miroshnychenko D, et al. Resistance to targeted therapies as a multifactorial, gradual adaptation to inhibitor specific selective pressures. Nat Commun [Internet]. 2020 May 14 [cited 2023 Jan 10];11(1):2393. Available from: https://pubmed.ncbi.nlm.nih.gov/32409712/